nature photonics

SUPPLEMENTARY INFORMATION
https://doi.org/10.1038/s41566-017-0053-8

In the format provided by the authors and unedited.

Three-dimensional holographic optical manipulation through a high-numerical-aperture soft-glass multimode fibre

Ivo T. Leite[1,2,3], Sergey Turtaev[1,3,4], Xin Jiang[5], Martin Šiler[6], Alfred Cuschieri[2], Philip St. J. Russell[5] and Tomáš Čižmár[1,3,6*]

[1]SUPA, School of Science and Engineering, University of Dundee, Nethergate, Dundee, UK. [2]Institute of Medical Science and Technology, University of Dundee, Dundee Medipark, Dundee, UK. [3]Leibniz Institute of Photonic Technology, Jena, Germany. [4]School of Life Sciences, University of Dundee, Nethergate, Dundee, UK. [5]Max Planck Institute for the Science of Light, Erlangen, Germany. [6]Institute of Scientific Instruments of the CAS, Brno, Czech Republic. *e-mail: tomas.cizmar@leibniz-ipht.de

3-D holographic optical manipulation through high-NA soft-glass multimode fibre

Ivo T. Leite[1,2,3], Sergey Turtaev[1,4], Xin Jiang[5], Martin Šiler[6], Alfred Cuschieri[2], Philip St.J. Russell[5], and Tomáš Čižmár[1,3,6*]

[1] *SUPA, School of Science and Engineering, University of Dundee, Nethergate, Dundee DD1 4HN, Scotland, United Kingdom*
[2] *Institute of Medical Science and Technology, University of Dundee, Dundee Medipark, Dundee DD2 1FD, Scotland, United Kingdom*
[3] *Leibniz Institute of Photonic Technology, Albert-Einstein-Straße 9, 07745 Jena, Germany*
[4] *School of Life Sciences, University of Dundee, Nethergate, Dundee DD1 4HN, Scotland, United Kingdom*
[5] *Max Planck Institute for the Science of Light, Staudtstraße 2, 91085 Erlangen, Germany*
[6] *Institute of Scientific Instruments of the CAS, Královopolská 147, 612 64 Brno, Czech Republic*
*****Corresponding author**: tomas.cizmar@leibniz-ipht.de

Supplementary Methods

1 Experimental setup

The experimental setup used in this work is depicted schematically in Fig. S1. It consists of two decoupled parts, the first dividing the laser beam into a signal and a reference beams and coupling them into single-mode polarisation-maintaining fibres (PMF1 and PMF2, respectively). Besides carrying the signal and reference beams to the main subset of the system, PMF1 and PMF2 serve also as Gaussian spatial filters. Lenses L1 and L2 form a telescope to demagnify the size of the beam originating from the laser source (Yb fibre laser, 1.064 µm wavelength, continuous wave), and half-wave plate HWP1 aligns its polarisation with the polarisation axis of the Faraday optical isolator OI. Half-wave plate HWP2 together with polarising beamsplitter cube PBS1 allow controlling the total amount of power propagating in the optical system (the excess power is diverted towards beam block BB), whereas half-wave plate HWP3 and polarising beamsplitter cube PBS2 allow adjusting the power ratio between the signal and reference beams, which are coupled into PMF1 and PMF2 via aspheric lenses L3 and L4, respectively.

The signal beam leaving PMF1 is collimated and expanded by lens L5 to overfill the spatial light modulator SLM under a small angle of incidence. Half-wave plate HWP4 is used to align the polarisation of the signal beam with the polarisation axis of the SLM. Aperture APT1, placed in the far-field of the SLM, isolates the first diffraction order while blocking all others. Lenses L6 and L7 are placed in a $4f$ configuration and image the first diffraction order of the holograms generated at the SLM onto dielectric mirror M1. Lens L8 and oil-immersion microscope objective MO1 are also placed in a $4f$ configuration and further relay the holograms from M1 to the input facet of the multimode fibre MMF. The combination of L6, L7, L8 and MO1 chosen ensures the necessary demagnification (370×) of the phase holograms such that their image size matches the dimensions of the MMF core. M1, being conveniently placed in a plane conjugate to the input fibre facet, serves as a steering mirror to finely adjust normal incidence onto MMF.

The distal end of MMF is immersed in a water droplet held by a custom-made cuvette (inset of Fig. S1) which is in contact with water-immersion microscope objective MO2 through a water-index-matching medium. MO2 in combination with tube lens L9 image the MMF output facet (or, in general, any desired calibration plane at a given distance from the endface) onto camera CCD1 with a magnification of 66×. MO2 is mounted on a piezo nanopositioner allowing a precise focussing adjustment, critical for the trap characterisation measurements as well as for the reconstruction of the 3-D profile of the focal points.

Quarter-wave plates QWP1 and QWP2 are used to convert the polarisation state of the signal beam from linear-to-circular and circular-to-linear, respectively, as circularly-polarised modes are shown to be better preserved upon propagation in MMFs [35].

Non-polarising beamsplitter cube BS combines the signal and reference beams at CCD1 for the interferometric measurement of the transmission matrix, as well as diverts a portion of the signal beam towards power detector PD allowing to assess the output power from MMF. Half-wave plate HWP5 is used to align the polarisations of the signal and reference beams to maximise the contrast in the interference patterns.

Dichroic mirror DCM placed in the optical path allows coupling incoherent light from LED1 into the fibre to provide uniform illumination on the trapped objects for *en face* imaging by CCD1, and short-pass filter SPF1 is placed to block the trapping beam. Lens L11 images aperture APT2 onto the back-focal plane of MO1. LED2, lenses L12 and L13, diffuser DIFF, and aperture APT3 provide a pseudo-Köhler illumination for side-view imaging by lens L14 onto camera CCD2. Short-pass filter SPF2 is used to filter out scattered light from the trapping beam.

Half-wave variable retarder HWVR is used to control the amount of power in the trap site (in closed-loop with feedback from PD) during the characterisation of the optical tweezers, as it allows introducing in the signal beam a polarisation component orthogonal to the polarisation axis of the SLM with variable amplitude, whose power remains in the zero diffraction order and is thus filtered out by APT1.

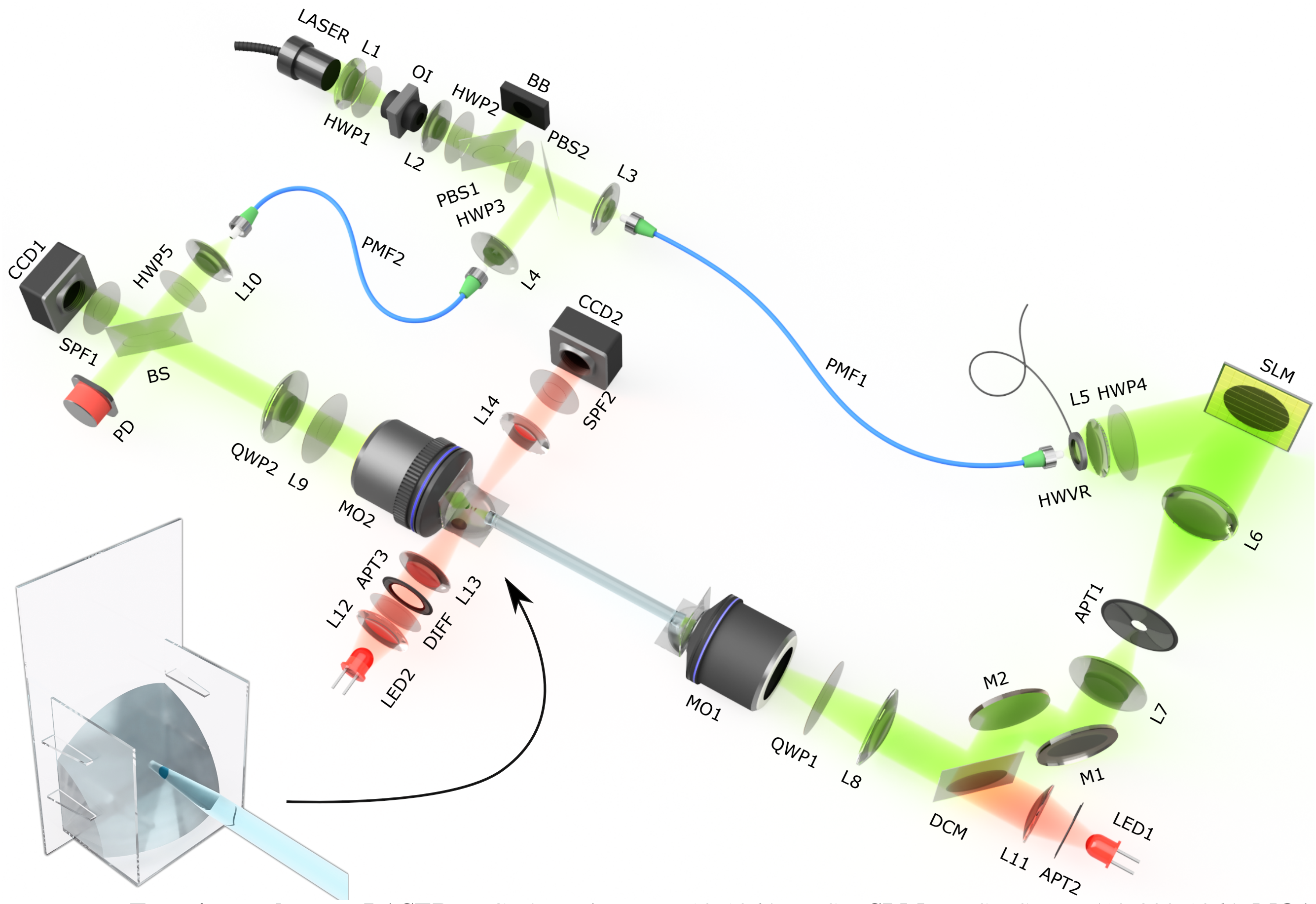

Figure S1 | **Experimental setup. LASER**: IPG Photonics YLR-10-1064-LP-SF; **SLM**: BNS HSPDM512-800-1064; **MO1**: Olympus UPlanFL 100x/1.30 Oil; **MO2**: Olympus UPlanSApo 60x/1.20 W mounted on Mad City Labs Nano-F100; **CCD1, CCD2**: Basler piA640-210gm; **PD**: Thorlabs S302C; **HWVR**: Thorlabs LCC1111-C; **LED1**: Thorlabs M625L3; **LED2**: Thorlabs MWWHL3; **OI**: LINOS FI-1060-8SI; **BB**: Thorlabs LB2; **PMF1, PMF2**: Thorlabs PM980-XP; **PBS1, PBS2**: Thorlabs PBS103; **BS**: Thorlabs BS011; **HWP1-HWP5**: Thorlabs WPMH10M-1064; **QWP1, QWP2**: Thorlabs WPMQ10M-1064; **DCM**: Thorlabs DMSP805R; **SPF1, SPF2**: Thorlabs FES0800; **APT1-APT3**: Thorlabs SM1D12D; **M1, M2**: Thorlabs BB1-E03; **DIFF:** Thorlabs DG10-220; **L1, L8, L9**: Thorlabs AC254-200-C; **L2**: Thorlabs AC254-100-C; **L3, L4**: Thorlabs C240TME-1064; **L5**: Thorlabs AC254-050-C; **L6**: Thorlabs AC254-250-C; **L7**: Thorlabs AC254-075-C; **L10**: Thorlabs C220TME-1064; **L11**: Thorlabs AC254-045-A; **L12**: Thorlabs AC254-030-C; **L13**: Thorlabs AC127-025-A; **L14**: Thorlabs C240TME-A;

2 Holographic methods

Measurement of the transmission matrix The phase holograms generated at a spatial light modulator (SLM) are imaged onto the input fibre facet in the off-axis holography configuration, where the first diffraction order is isolated using a spatial filter. In order to measure the transmission matrix (TM) of the fibre, a calibration plane (at a given distance from the output fibre facet) is imaged onto a CCD detector, and an external phase reference is introduced in the optical pathway via a non-polarising beamsplitter. We have chosen a set of 38×38 orthogonal plane waves as the basis of input modes, whereas the output modes are heavily oversampled, consisting of a square grid of 100×100 points at the calibration plane which are conjugate to individual pixels in the CCD detector.

The input and output modes, $\Psi^{\text{in}}_{k,l}$ and $\Psi^{\text{out}}_{u,v}$, are connected via a matrix of complex coefficients:

$$\Psi^{\text{out}}_{u,v} = \sum_{k,l} t^{k,l}_{u,v} \Psi^{\text{in}}_{k,l}, \tag{S1}$$

where k and l are the position indices in Fourier space of the input modes $(k,l = -19,\ldots,18)$, and u and v are the position indices of the output modes in the calibration plane $(u,v = 1,\ldots,100)$. Each element $t^{k,l}_{u,v}$ of the transmission matrix can be represented in the polar form as:

$$t^{k,l}_{u,v} = |t^{k,l}_{u,v}| e^{i\phi^{k,l}_{u,v}}, \tag{S2}$$

where $i = \sqrt{-1}$ is the imaginary unit, the amplitude $|t^{u,v}_{k,l}|$ is a positive array and the phase $\phi_{k,l}^{u,v}$ has real values in the interval $[-\pi,\pi]$.

Using the SLM to change the phase difference $\Delta\phi$ between a given input mode (k',l') and the external phase reference leads to a harmonic signal of the intensity $I_{u,v}^{k',l'}$ in each position of the grid of output modes:

$$I_{u,v}^{k',l'} = |t_{u,v}^{k',l'}\Psi_{k',l'}^{\text{in}} \cdot e^{i\Delta\phi} + \Psi^{\text{ref}}|^2. \tag{S3}$$

Since we measure TM in the basis of input modes $\Psi_{k,l}^{\text{in}}$, then in this representation we have $|\Psi_{k',l'}^{\text{in}}| = 1$ and $\phi_{k',l'}^{\text{in}} = 0$ for the amplitude and phase of probed input mode. Expanding the previous equation leads to:

$$I_{u,v}^{k',l'} = |t_{u,v}^{k',l'}|^2 + |\Psi^{\text{ref}}|^2 + 2|t_{u,v}^{k',l'}||\Psi^{\text{ref}}|\cos(\phi_{u,v}^{k',l'} - \phi^{\text{ref}} + \Delta\phi), \tag{S4}$$

where ϕ^{ref} is the phase of the reference signal. Thus the complex field (i.e. both amplitude and phase) at each position (u,v) of the calibration plane can be retrieved by changing the phase difference $\Delta\phi_q$ in n steps using the recorded intensity $(I_{u,v}^{k',l'})_q$ for each step:

$$\sum_{q=1}^{n} (I_{u,v}^{k',l'})_q e^{i\Delta\phi_q} = 2|t_{u,v}^{k',l'}||\Psi^{\text{ref}}|e^{i(\phi_{u,v}^{k',l'} - \phi^{\text{ref}})}, \tag{S5}$$

where in our case $\Delta\phi_q = q\pi/2$ and $n = 8$, corresponding to changing the phase in steps of $\pi/2$ over two phase periods. This is equivalent to measure the row (k',l') of the TM since the reference signal is assumed to have uniform amplitude $|\Psi^{\text{ref}}|$ across the grid (u,v) of output modes.

Acquiring the full TM corresponds to repeating this procedure for all combinations of (k,l). This procedure takes around 30 min, during which the reference phase usually experiences variations due to an unavoidable degree of instability in the system, which translates into an error in the measurement of $\phi_{u,v}^{k,l}$. This can be compensated by tracking the phase reference drift, which we have implemented as follows. For each input mode (k',l') probed, we record $n+1$ interference patterns, the extra one always corresponding to a given input mode (k_0,l_0). This intensity pattern $I_{u,v}^{k_0,l_0}$ is compared to the first one acquired, $\bar{I}_{u,v}^{k_0,l_0}$, with ϕ^{ref} chosen as the value minimising:

$$\sum_{u,v} \left(I_{u,v}^{k_0,l_0} \cos\phi^{\text{ref}} - \bar{I}_{u,v}^{k_0,l_0} \right)^2. \tag{S6}$$

Measuring the mode-dependent loss Due to the strong mode-dependent loss (MDL) inherent to the multimode fibre used, different mode-groups (i.e. waveguide modes having similar propagation constants) experience distinct degrees of attenuation upon propagation. This translates into a non-uniform power distribution in the spectrum of the output modes which limits the available NA, as illustrated schematically in Fig. 1 in the main text. In order to pre-compensate the MDL we couple into the fibre all input plane-wave modes, labelled as (k,l), and integrate the output

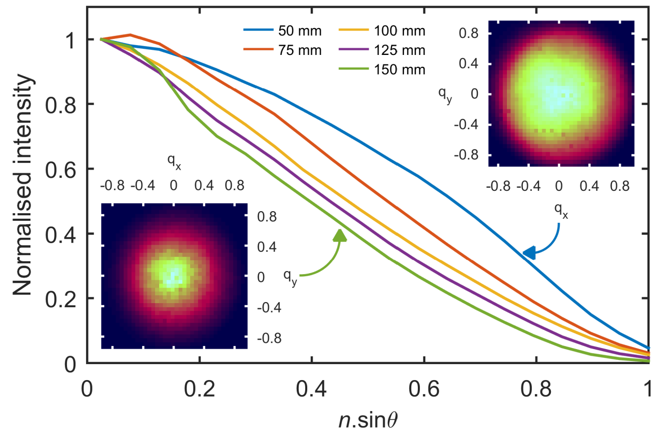

Figure S2 | Measurements of the mode-dependent loss. Azimuthally averaged measurements of the mode-dependent transmission for fibre segments of varying length, from 50 mm to 150 mm. The inset figures show normalised measurements of the spatial-frequency dependent intensity for fibres with length 50 mm (top-right) and 150 mm (bottom-left).

power at the CCD for each one of them. This allows measuring the intensity map $I^{k,l}$, which we normalise to the maximum value, containing the information of the optical transmittance of the different mode groups. Figure S2 shows the azimuthally-averaged intensity distribution $I^{k,l}$ for different fibre lengths, as a function of the normalised spatial frequency $n\sin\theta = k_t/k_0$, where $k_t = \sqrt{k_x^2 + k_y^2}$ is the transverse component of the wave-vector and $k_0 = 2\pi/\lambda$ its magnitude *in vacuo*. The insets in Fig. S2 display the mode-dependent transmission $I^{k,l}$ measured for the longest and shortest fibres (150 mm and 50 mm long), as a function of the normalised spatial frequencies $q_{x,y} = k_{x,y}/k_0$.

Generating a single diffraction-limited focus The liquid-crystal spatial light modulator (SLM) used allows for the generation of phase-only holograms. To generate a diffraction-limited output mode at a particular position (u',v') in the calibration plane, only the phase information is used, i.e. we apply the phase-only modulation:

$$H(u',v') = \arg\left(\mathscr{F}^{-1}\left[t_{u',v'}^{k,l}\right]\right), \tag{S7}$$

where $\mathscr{F}^{-1}$ denotes the inverse Fourier transform, implemented using a fast Fourier transform (FFT) algorithm. The fact that we use phase-only modulation instead of the measured complex modulation (i.e. amplitude and phase) results in a noisy background, as only $\pi/4 \simeq 78.5\%$ of the output power can be controlled in this manner [29]. On the other hand, the implementation of amplitude modulation would involve further power loss and decrease the overall efficiency, thus reducing the available output power which is crucial for the optical trapping.

Simultaneous generation of multiple foci To generate multiple diffraction-limited foci simultaneously at the output positions (u_q,v_q), where $q = 1,\ldots,N$ is the index of each output mode (N is the total number of output foci), we apply to the SLM the phase-only information of the complex superposition of the complex modulations:

$$H^N = \arg\left(\sum_{q=1}^{N} \sqrt{a_q}\mathscr{F}^{-1}\left[t^{k,l}_{u_q,v_q}\right]\right), \tag{S8}$$

where a_q are the required intensity contributions for the composition of output modes, with $\sum_{q=1}^{N} a_q = 1$. To pre-compensate the MDL, this design of the system allows to perform spectral amplitude modulation, implemented as:

$$H^N = \arg\left(\sum_{q=1}^{N} \sqrt{a_q}\mathscr{F}^{-1}\left[\frac{1}{\sqrt{I^{k,l}}}t^{k,l}_{u_q,v_q}\right]\right). \tag{S9}$$

Axial control of generated foci Owing to the remarkable cylindrical symmetry of fibre-optic waveguides, the longitudinal component of the wavevector (i.e. the propagation constant) is very well conserved through the fibre (axial memory effect) [31]. Thus, a quadratic phase added to the spatial spectrum of the input modes is preserved and, therefore, found in the spatial spectrum of the output modes, resulting in a defocus and axial displacement of the diffraction-limited foci. For a single output focus located at (u',v'):

$$H(u',v') = \arg\left(\mathscr{F}^{-1}\left[t^{k,l}_{u',v'}e^{ib(k^2+l^2)}\right]\right), \tag{S10}$$

where b is a scalar whose magnitude gives the amount of defocussing, and whose sign defines the direction of defocussing ($b > 0$ produces a negative defocus, towards the fibre facet, while $b < 0$ gives rise to a positive defocus away from the fibre facet). More generally, when generating multiple output FP modes simultaneously while also pre-compensating the MDL, a defocus can be applied to each of them individually as:

$$H^N = \arg\left(\sum_{q=1}^{N} \sqrt{a_q}\mathscr{F}^{-1}\left[\frac{1}{\sqrt{I^{k,l}}}t^{k,l}_{u_q,v_q}e^{ib_q(k^2+l^2)}\right]\right). \tag{S11}$$

Nanometre-scale positioning Since the separation between the calibrated sites of the grid of output modes is much smaller than the spatial extent (spot-size) of each one of them, the fine positioning of a distal FP mode between such calibrated locations can be achieved by generating two consecutive modes simultaneously, say (u',v') and $(u'+1,v')$, by applying to the SLM the phase-only modulation:

$$H = \arg\left(a\mathscr{F}^{-1}\left[\frac{t^{k,l}_{u',v'}}{\sqrt{I^{k,l}}}\right] + (1-a)\,\mathscr{F}^{-1}\left[\frac{t^{k,l}_{u'+1,v'}e^{i\delta}}{\sqrt{I^{k,l}}}\right]\right), \tag{S12}$$

where δ is the phase delay between the two output modes – which needs to be compensated for them to interfere constructively – given by:

$$\delta = \arg\left(\sum_{k,l}(t^{k,l}_{u',v'})^* \cdot t^{k,l}_{u'+1,v'}\right), \tag{S13}$$

where * denotes the complex conjugate. The modulation in Eq. (4) results in a distribution of the optical field corresponding to a single FP whose central position can be finely tuned by the relative amplitude a of the two output modes.

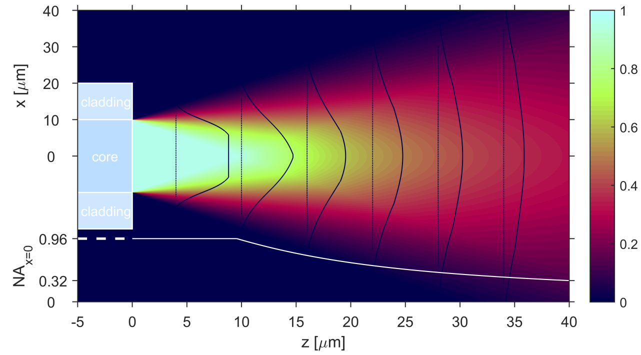

Figure S3 | Numerical aperture of sample modes at different distances from the output fibre facet. The lower plot shows the evolution of the NA along the optical axis and the series of dark subplots illustrate the NA profiles across different axial planes in front of the fibre.

Supplementary Results

1 Available high-NA volume

Figure S3 shows the available NA in front of the output fibre endface, estimated in the ray-optics approximation using the parameters $\mathrm{NA_{fibre}} = 0.96$ and core diameter $d = 20\,\mu\mathrm{m}$ for the fibre and $n = 1.333$ (water) for the refractive index of the surrounding medium. The lower plot shows the evolution of the on-axis NA with increasing distance z from the fibre, given by:

$$\mathrm{NA} = \min\left\{\mathrm{NA_{fibre}}, n\sin\left[\tan^{-1}\left(\frac{d/2}{z}\right)\right]\right\}. \tag{S14}$$

The available NA is maximum in a conical region in front of the fibre endface whose apex is at a distance of approximately 10 μm from the fibre. Accordingly, the volume in front of the fibre facet where the NA is maximum is approximately $1000\,\mu\mathrm{m}^3$. The trapping experiments were performed with the calibration plane located at a distance $z \simeq 4\,\mu\mathrm{m}$ from the fibre facet (represented in Fig. S3 as the left-most NA axial profile) to allow for access of the particles as well as manipulation depth in the axial direction. At this distance, the region in which the NA is maximum is about 12 μm in diameter.

2 Minimum NA for stable trapping

In order to model the trapping properties of light focused by the high NA optical fibre we firstly used an angular spectrum decomposition in order to describe the intensity profile close to the beam focus. The angular spectrum description of light focusing through an objective lens corresponds to the Debye approximation of the diffraction of a convergent spherical wave on a circular aperture [51,52]. The components of the electric field vector polarised along the x axis are given as:

$$E_x(x,y,z) = -\frac{\mathrm{i}}{2}k\left(I_0 + I_2\frac{x^2-y^2}{x^2+y^2}\right), \quad \text{(S15)}$$

$$E_y(x,y,z) = -\mathrm{i}kI_2\frac{xy}{x^2+y^2}, \quad \text{(S16)}$$

$$E_z(x,y,z) = -kI_1\frac{x}{\sqrt{x^2+y^2}}, \quad \text{(S17)}$$

where

$$I_0(r,z) = \int_0^{\Theta} A(\alpha)\sin\alpha\,(1+\cos\alpha)\,J_0(kr\sin\alpha) \times \exp(\mathrm{i}kz\cos\alpha)\mathrm{d}\alpha, \quad \text{(S18)}$$

$$I_1(r,z) = \int_0^{\Theta} A(\alpha)\sin^2\alpha\,J_1(kr\sin\alpha) \times \exp(\mathrm{i}kz\cos\alpha)\mathrm{d}\alpha, \quad \text{(S19)}$$

$$I_2(r,z) = \int_0^{\Theta} A(\alpha)\sin\alpha\,(1-\cos\alpha)\,J_2(kr\sin\alpha) \times \exp(\mathrm{i}kz\cos\alpha)\mathrm{d}\alpha, \quad \text{(S20)}$$

and $r=\sqrt{x^2+y^2}$ denotes the radial distance from the optical axis z, $k=2\pi n/\lambda_{\mathrm{vac}}$ is the wave vector (n being refractive index of surrounding medium and λ_{vac} vacuum wavelength of the trapping beam), and Θ is the angular aperture of the focusing optics that is connected to the fibre numerical aperture by $\mathrm{NA}_{\mathrm{fibre}} = n\sin\Theta$. Furthermore, J_ν denotes the Bessel function of the first kind and ν-th order, and the angular amplitude distribution in the aplanatic projection follows [51]

$$A(\alpha) = A_0\sqrt{\cos\alpha}. \quad \text{(S21)}$$

Constant A_0 corresponds to the focusing of a plane wave, however, as the energy distribution of the light is not uniform over all angles in our case we employed an apodization function parametrized by the filling factor f_0 [52], i.e.

$$A(\alpha) = A_0\exp\left(-\frac{1}{f_0^2}\frac{\sin^2\alpha}{\sin^2\Theta}\right)\sqrt{\cos\alpha}. \quad \text{(S22)}$$

The circularly polarised beam is realised by the interference of two beams that are linearly polarised along the x and y axes with a mutual phase shift of $\pi/2$. A_0 is obtained from the beam power. We determined the Airy disk diameter for a wide range of f_0 using the procedure described below (see Supplementary Results 3) and, further, we obtained the effective NA as a function of the filling factor, see inset of Fig. S4.

In the next step we calculated the optical forces acting on a silica bead ($n_{\mathrm{silica}} = 1.45$, 1.57 µm diameter) immersed in water that is placed into various axial locations. Using the force curves we checked the existence of a trapping location, the trap stiffness $\kappa = -\partial F/\partial z$ and the depth of the potential well ΔU. First, let us mention that no trapping location exists for filling factors $f_0 < 0.4$ that correspond to an effective NA of 0.6. However, for low NA (under 0.74) the trapping depth is quite shallow and the particle escapes the trapping region by the random motion in less than a second. The long term time stability might be evaluated in the means of passage times or in our case by the Kramers' time [53]

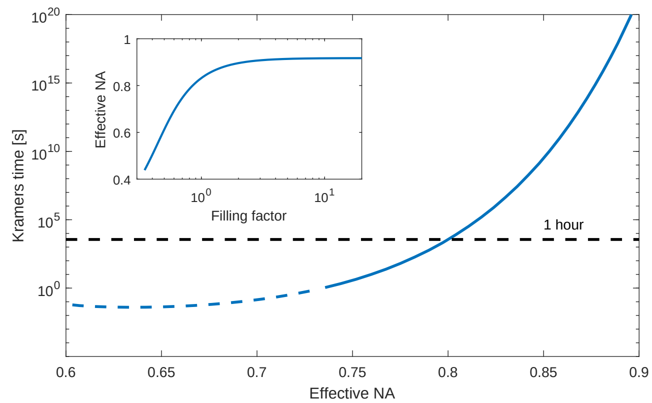

Figure S4 | **Minimum NA for stable trapping.** Kramers time of residence of a silica particle in the optical trap (blue curve) as a function of trap effective NA. The dashed portion of the blue curve depicts the region in effective NA where $\tau_K < 1$ s and the black dashed line marks 1 hour limit. The inset figure shows the effective NA as a function of filling factor f_0.

$$\tau_K = \frac{2\pi\beta}{\sqrt{|\kappa\kappa_{\mathrm{edge}}|}}\exp\left(\frac{\Delta U}{k_B T}\right), \quad \text{(S23)}$$

where β is the hydrodynamic drag, κ is the trap stiffness, κ_{edge} is the stiffness (force differential) at the trap edge and k_B and T are the Boltzmann constant and thermodynamic temperature. Figure S4 shows the Kramers' time τ_K as a function of effective NA. The blue curve depicts the Kramers' time calculated for a trapping power of 1 mW, and the dashed part of this curve marks region of $\tau_K < 1$ s. Additionally, the black dashed line marks the Kramers time of 1 h, i.e. the limit where we may consider the trapping stable enough in order to perform long term observation of the trapped object. One may see that this happens for effective NAs larger than 0.80.

3 High-resolution focussing

The generation of high NA, diffraction-limited foci is of central importance in this work, as it the enabling principle for HOT providing 3D optical confinement, but also forms the basis for other high NA techniques including imaging. To assess the achievable NA of the system as well as the impact of the MDL compensation, we have carried out a study where 91 focal-point (FP) modes are sequentially generated across the distal fibre facet for each measurement of the TM. The procedure was repeated for several TM measurements and for varying length of the same fibre segment which was successively re-cleaved to reduce its size in increments of 25 mm.

Since the intensity distribution of each FP mode spans over the 8-bit dynamic range of the CCD camera, three images are taken for each FP mode with exposure times of 0.1 ms, 1 ms, and 10 ms in order to reconstruct its intensity distribution $I(x,y)$,

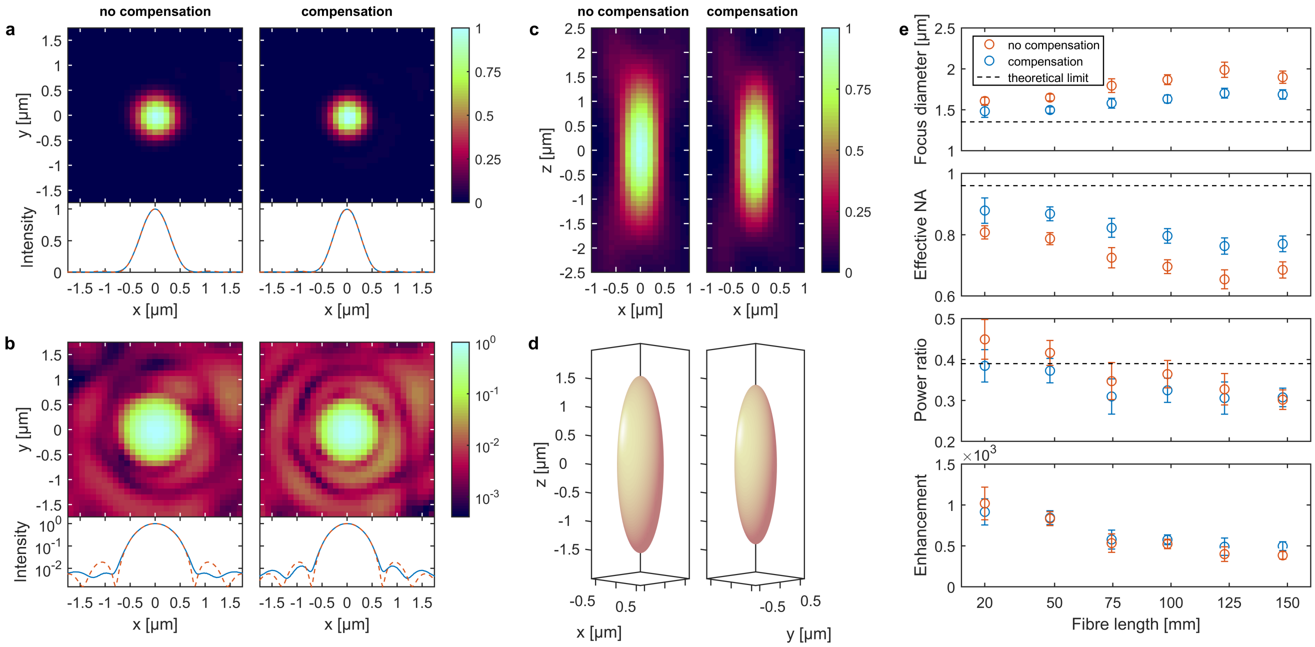

Figure S5 | **High-resolution focussing through MMFs. a,b,** Transverse intensity profile of a focal-point (FP) mode, with and without MDL compensation, and comparison of the azimuthally-averaged intensity profile with the fitted Airy disk intensity distribution. The NA of the FP mode is enhanced from 0.82 ± 0.01 (prior to MDL compensation) up to 0.91 ± 0.01 (after MDL compensation). **c,** Longitudinal profile of the intensity distribution of the same FP mode. **d,** Ellipsoid fitted to the level surface with intensity corresponding to $1/e$ of the maximum value. The fibre used in **(a-d)** was 50 mm long. **e,** Influence of the MDL compensation on the Airy disk diameter, effective NA, power ratio, and enhancement for varying length of the MMF.

where x and y denote the Cartesian coordinates of the image in pixel units. One of such intensity distributions is shown in Fig. S5a,b, prior and after MDL compensation, which is the same as shown in Fig. 1d in the main text. The FP mode shown was generated at a radial distance 2.25 µm (from the fibre axis) and distance 2.0 µm from the fibre facet, through a 50 mm long fibre. Each intensity distribution $I(x,y)$ is fitted to a 2-D Airy disk distribution:

$$f(x,y) = a\left(\frac{2J_1(\rho)}{\rho}\right)^2 + b, \tag{S24}$$

where J_1 is the Bessel function of the first kind of order one, and

$$\rho = \frac{\sqrt{(x-c)^2+(y-d)^2}}{e}, \tag{S25}$$

with a, b, c, d, and e being free parameters (a measures the amplitude, b the average speckled background, c and d the Cartesian coordinates of the centre of the distribution, and e its width). In Fig. S5a,b, as well as in the main text Fig. 1e, the fitted distribution $f(x,y)$ is compared with the azimuthally averaged $I(x,y)$. With the knowledge of the pixel size in the CCD (7.4 µm) and the calibrated magnification of the *en face* imaging pathway (66×), the diameter of the Airy disk, taken as first-zero-ring in Eq. (S24), can be estimated as $d_{\text{Airy}} = 2\cdot 3.8317\cdot 7.4\,\mu\text{m}\cdot e/66$. The corresponding effective NA can then be retrieved as $\text{NA} = {}^{1.22\lambda}/_{d_{\text{Airy}}}$, where λ is the wavelength in free space (1064 nm).

By scanning the imaging objective axially in steps of 100 nm, we were able to reconstruct the 3-D intensity profile of the FP mode shown in Fig. S5a,b. Figure S5c shows the longitudinal profile of the FP mode, where the spot size in the axial direction is approximately 3.8 times larger than its lateral dimension, both with and without MDL compensation. Figure S5d shows the 3-D structure of this FP mode as an ellipsoid fitted to the level surface corresponding to ${}^1/_e$ of the maximum intensity.

In addition to the achievable NA, which determines the volumetric confinement of light, other parameters quantifying the uncontrolled background are also important in view of proposed applications. The *power ratio* is the fraction of total output power at the distal fibre facet which is contained in the FP mode, and can be estimated as $\gamma^2 = \sum_{x,y}[f(x,y)-b]/\sum_{x,y}I(x,y)$. The *enhancement* is defined as the ratio between the maximum intensity of the generated FP mode and the average speckled background, which can be calculated as $\eta = {}^{a+b}/_b \simeq {}^a/_b$. Figure S5e summarises the results of this study, showing the focus diameter (defined as the first zero-ring in the Airy disk), effective NA, power ratio, and enhancement for each fibre length tested. Our MDL-compensation increases the NA in average by 0.09. However, the ability to generate FP modes with higher NA decreases with increasing fibre lengths. As the optical loss grows exponentially with the fibre length, the transmitted power by the higher-order group modes becomes comparable to the noise level in case of the longer fibres.

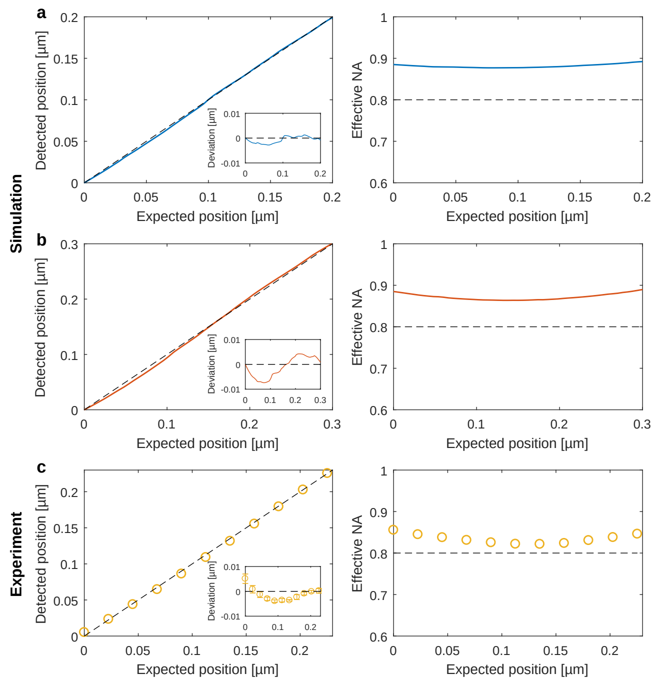

Figure S6 | Fine positioning of HOT. Detected central position and effective NA of a focus created by coherent superposition of two neighbouring FP output modes as a function of its expected central position. **a,b,** Simulated data using a FP separation of **(a)** 0.2 µm and **(b)** 0.3 µm. **c,** Experimental data with consecutive FP modes spaced by 0.23 µm. The errorbars in **(c)** are smaller than the data markers. The horizontal dashed line indicates the NA value of 0.8 required for stable optical confinement and the inset figures show the deviation between the detected and expected positions of the focus as it is relocated between the two FPs.

This translates into increasingly larger errors in the measurement of the MDL, thus limiting the efficiency of the compensation for the higher spatial frequencies which leads to a decreasing available NA with increasing fibre length. The power ratio across all fibre lengths is around $(33 \pm 4)\%$ with and $(37 \pm 5\%)$ without MDL compensation. This means that, in the HOT characterisation experiments, about 67% of the measured power is distributed as background outwith the trap site. We note that the theoretical limit for the power ratio in the case of phase-only modulation is shown to be $\pi/4 \simeq 78.5\%$ [29]. However, in the presence of complete polarisation mixing, and if only one polarisation state is controlled (as in this work) this value is further reduced by half, being $\pi/8 \simeq 39.3\%$ – a value in agreement with the experiments.

4 Fine positioning of the HOT

As explained in the main text, in order to reposition the HOT with nanometric precision to locations between calibrated FP modes, we weight the relative amplitudes of two neighbouring FPs generated simultaneously as described by Eq. (S12). Naturally, this procedure works when the separation between the FPs is much smaller than their spatial extent (spot size), while as the FP separation approaches their size the generated focus broadens, translating into a decreasing NA and stiffness of the HOT. To verify the limits of this approach, we have simulated the focus relocation for FP separations ranging from 0.1 µm to 0.8 µm using a TM calculated for a fibre having the same parameters as those used in our experiments (see Supplementary Media SM6). The resulting intensity distribution is fitted to an Airy disk distribution deformed elliptically, allowing us to retrieve the actual position of the focus as well as its effective NA (in the direction of the major axis, i.e. parallel to the line segment connecting the two FPs) as it is relocated. The results of the simulations for the FP separations of 0.2 µm and 0.3 µm are shown in Fig. S6a,b. We have complemented these simulations with experimental measurements where the spacing between consecutive is ≈0.23 µm. At each position, the intensity distribution of the relocated focus was reconstructed from three images taken at three distinct exposure times (as detailed in Supplementary Results 3) and fitted to an elliptical Airy disk as in the simulations. Figure S6c shows the experimental data averaged over five measurements. For the 0.23 µm FP separation used in this work, we see that the effective NA is almost kept constant during the HOT fine positioning, and the total deviation from the expected trajectory is smaller than 5 nm. Moreover, the precision of each step along the trajectory is 1.8 nm for the step size used (23 nm). It is worth noting that the presence of MDL in the 65 mm-long fibre used in the measurements, not taken into account in the simulations, is responsible for a visibly smaller effective NA in the measurements when compared with the simulated data.

5 Demonstration of HOT resilience to fibre bending

In practical applications of HOT delivered *in vivo* by a MMF, a certain degree of bending may be unavoidable, for instance due to mechanical stress induced by the surrounding tissue or to the dynamic nature of living specimens (e.g. due to breathing, heart beating, etc.). To demonstrate the HOT's resilience to bending of the fibre, we have conducted an experiment in which a 65 mm long fibre is subject to bending while trapping a silica microsphere. The bending occurs in the unheld distal segment of the fibre (≈15 mm long) by means of a controlled pressure applied near the fibre endface by a motorised stage moving upwards, as depicted in Fig. S7. The side-view recording of the experiment is shown in Supplementary Media SM5. Notably, the particle remained confined by the HOT even when the fibre endface was translated by 2 mm, the maximum allowed by the conditions of the experiment, thus introducing a radius of curvature of 5 cm.

6 Effect of temperature on the transmission matrix

Power absorption in the MMF leads to an increase in its temperature which modifies the measured TM. This was seen in the characterisation of the optical tweezers, where the increasing optical power causes the trap site to displace axially by a few microme-

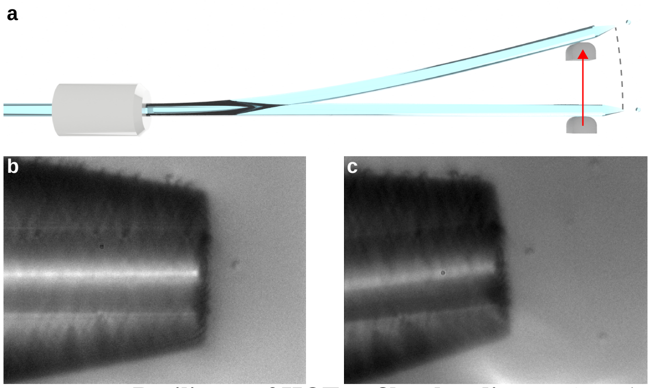

Figure S7 | **Resilience of HOT to fibre bending. a,** A static HOT confining a silica microsphere (1.5 μm diameter) is delivered through a fibre with length 65 mm. The unheld distal portion of the fibre (15 mm long) is initially straight and is then progressively bent due to the force applied by a motorised stage moving upwards. **b,** Side-view image of the trapped particle in the initial, straight conformation of the fibre. **c,** Side-view image of the trapped particle in the final, bent conformation of the fibre corresponding to a vertical displacement of 2 mm and a radius of curvature of 5 cm.

tres (Fig. S8c). Remarkably, in the first instance the quality of trap is seen to be well preserved as the trap stiffness increases linearly with the optical power, especially in the case of fibres with a length smaller than 100 mm (main text Fig. 4). This lead to the hypothesis that, in the first instance, the optical absorption gives rise to a defocus of the focal point (FP) modes, and further increasing power leads to the degradation of the TM.

To test this, we measured the TM of a ≈ 170 mm long fibre under varying temperature. With respect to the system shown in Fig. S1, the setup was modified into an upright configuration with the fibre bent 180° between the two microscope objectives at the bottom. This allowed immersing ≈ 100 mm of the fibre in a thermal bath whose temperature was controlled in closed-loop and could be kept constant with precision down to 0.01 °C.

Comparing the several TM measurements at different temperatures with the one obtained at room temperature ($T = 21.84$ °C) we found that to generate the same distal FP modes, the proximal far-field is modified by a quadratic phase – a defocus – with magnitude proportional to the temperature difference. Figure S8a shows this phase difference, averaged for all distal FPs in each measurement of the TM, and compares it with a fitted quadratic phase. Figure S8b shows that the dependence of averaged defocus with temperature is very linear, having a slope of $\approx 0.19\lambda/$°C for the fibre length used. A temperature increase can therefore be compensated to some extent by applying a defocus on the proximal field, without the need for re-measuring the TM. Conversely, if we retain the same TM measurement without modifying the proximal field, such defocus will manifest in the distal field as an axial displacement of the FP modes generated.

In order to link the defocus due to power absorption with the temperature increase, a study of the axial displacement of a confined particle as a function of the optical power was conducted using a fibre of similar length (150 mm). This dependence, shown in Fig. S8c, is also very linear with a slope of $\approx 0.065\lambda/$mW. Although the temperature is not distributed uniformly along the fibre, these two studies gave us a coarse estimate that the fibre temperature increases by $\approx$0.3 °C per mW, for the fibre length used.

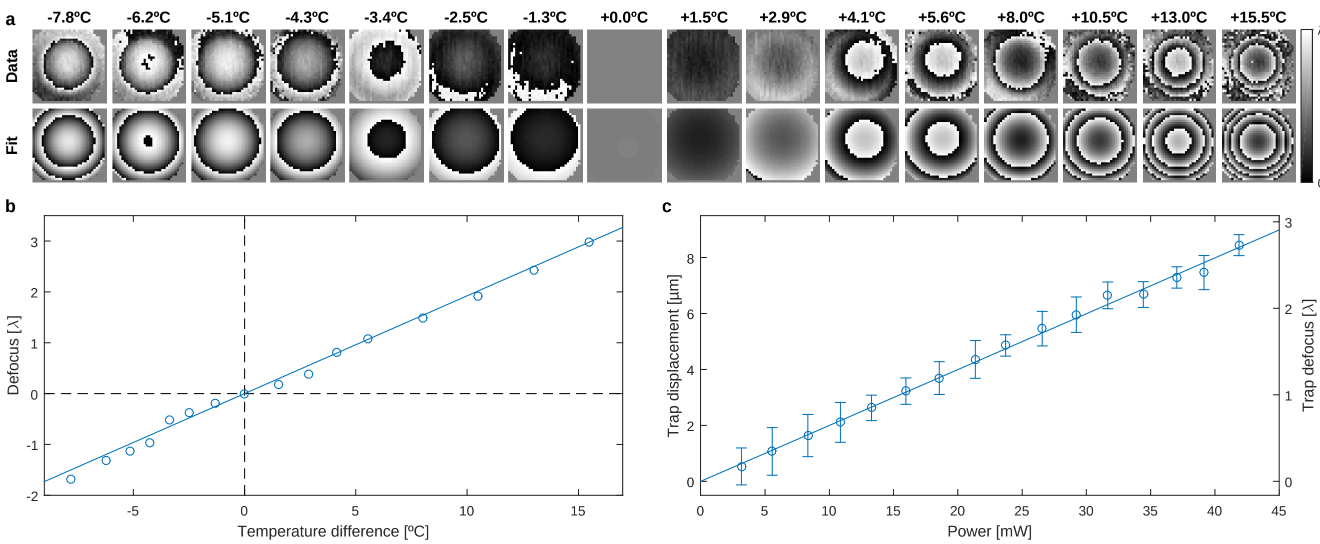

Figure S8 | **Effect of temperature on the transmission matrix. a,** Phase difference in the proximal far-field with respect to the TM measurement at room temperature, and fit to a quadratic phase. **b,** Corresponding defocus (in units of wavelength) as a function of the temperature difference. **c,** Axial displacement of the trap site and corresponding defocus during the optical tweezers characterisation for a fibre with length 150 mm.

Supplementary Figures

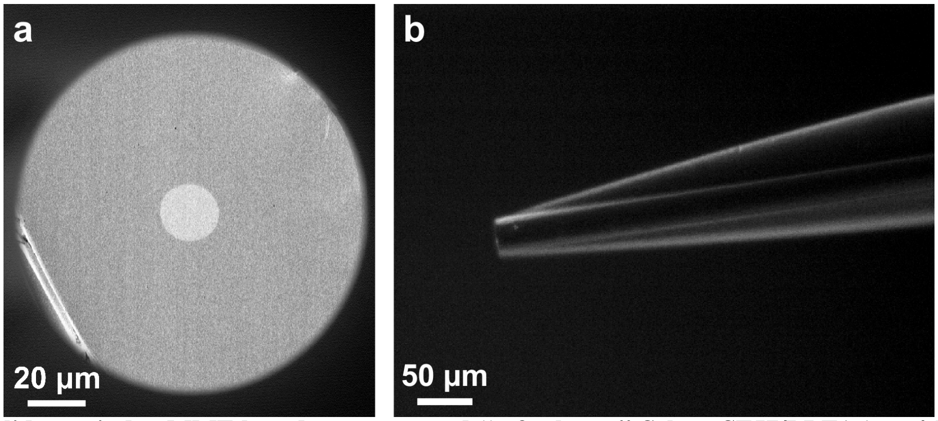

Figure S9 | **All-solid step-index MMF based on compound "soft-glasses" Schott SF57/LLF1 (core/cladding). a,** SEM image of the fibre endface. The diameters of the core and of the cladding are 20 µm and 125 µm, respectively. **b,** Micrograph of a post-processed fibre probe where the cladding thickness has been reduced to 35 µm (at the tip) by side-polishing.

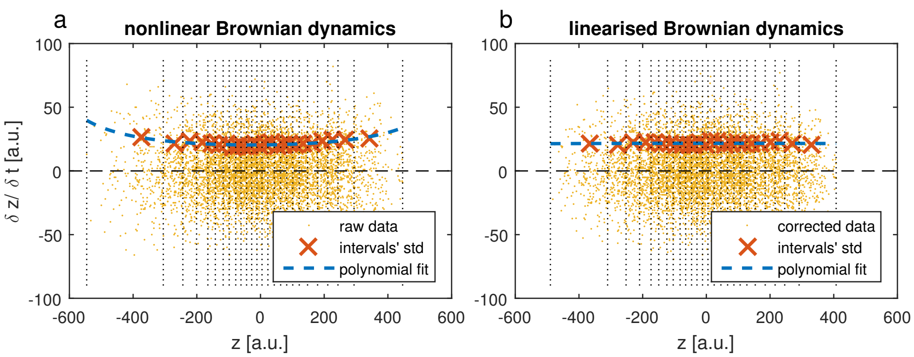

Figure S10 | **Linearisation of z-trajectory. a,** Varying Brownian motion along the z-trajectory (yellow points), standard deviation for each interval (red '×' markers) and their polynomial fit. **b,** Analogous study on linearised z-trajectory.

Supplementary Media

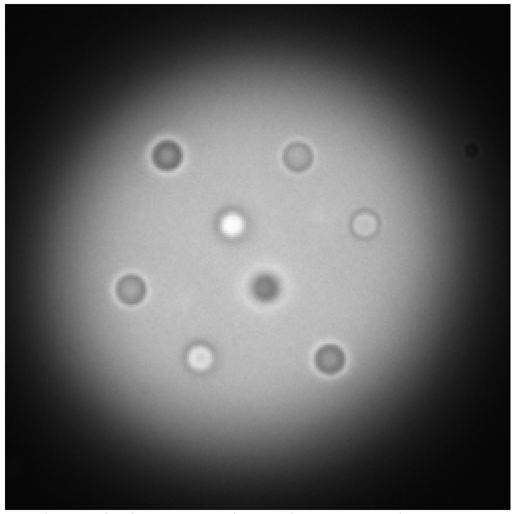

Figure SM1 | **Dynamic HOT manipulation of eight particles in a rotating cube arrangement.** The particles are silica microspheres with diameter 1.5 µm in a water suspension. The particles appearing 'brighter' are at a greater axial distance from the fibre facet. The video playback speed has been increased.

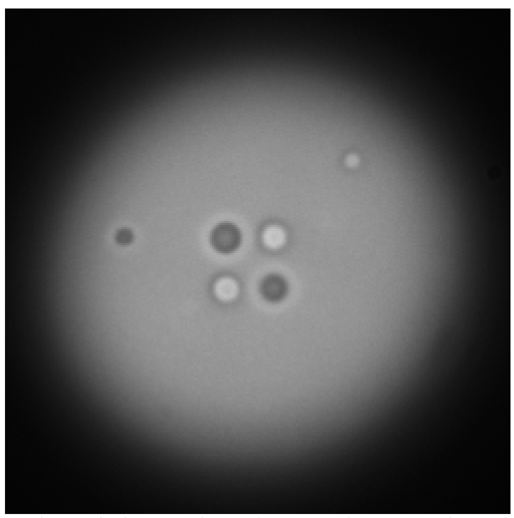

Figure SM2 | **Dynamic HOT manipulation of six particles illustrating Bohr's model of the He atom.** The particles are silica microspheres with diameter 1.5 µm (the four particles in the 'nucleus') and 1 µm (the two orbiting 'electrons') in a water suspension. The particles appearing 'brighter' are at a greater axial distance from the fibre facet. The video playback speed has been increased.

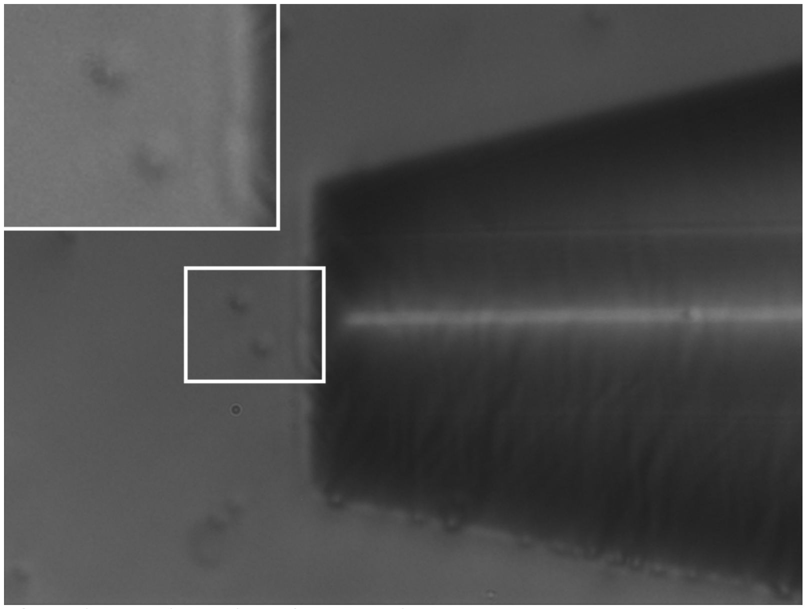

Figure SM3 | **Dynamic HOT axial manipulation of two particles.** The particles are silica microspheres with diameter 1.5 µm in a water suspension. The inset in the video shows the magnified region of interest. The video playback speed has been increased.

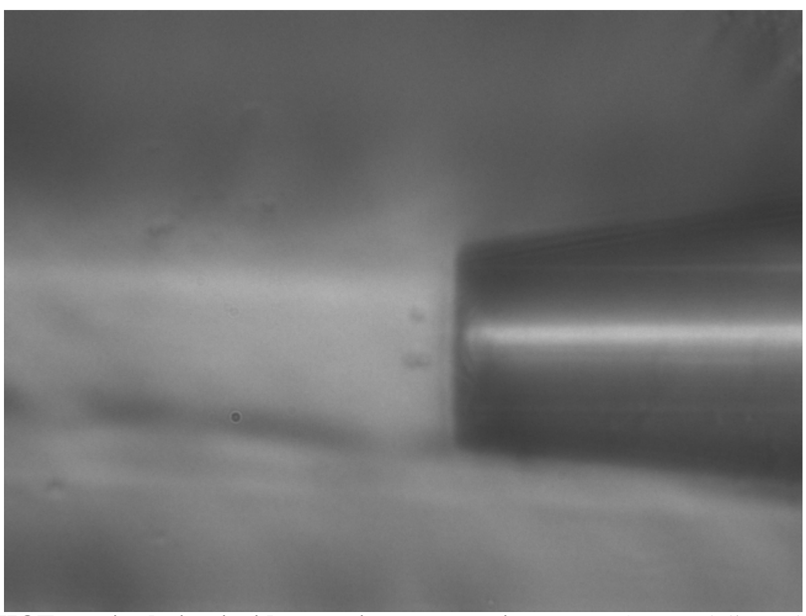

Figure SM4 | **Dynamic HOT manipulation inside a semi-opaque cavity.** Two HOT are delivered inside a turbid cavity by a MMF via a small opening ($\sim$ 125 µm wide). One particle is confined in the first trap, and two particles are confined in the second trap. The traps are separated by $\sim$ 5 µm laterally (i.e. in the direction perpendicular to the image plane) and are displaced vertically during insertion and removal of the MMF. The particles are silica microspheres with diameter 1.5 µm in a water suspension. The video playback speed has been increased.

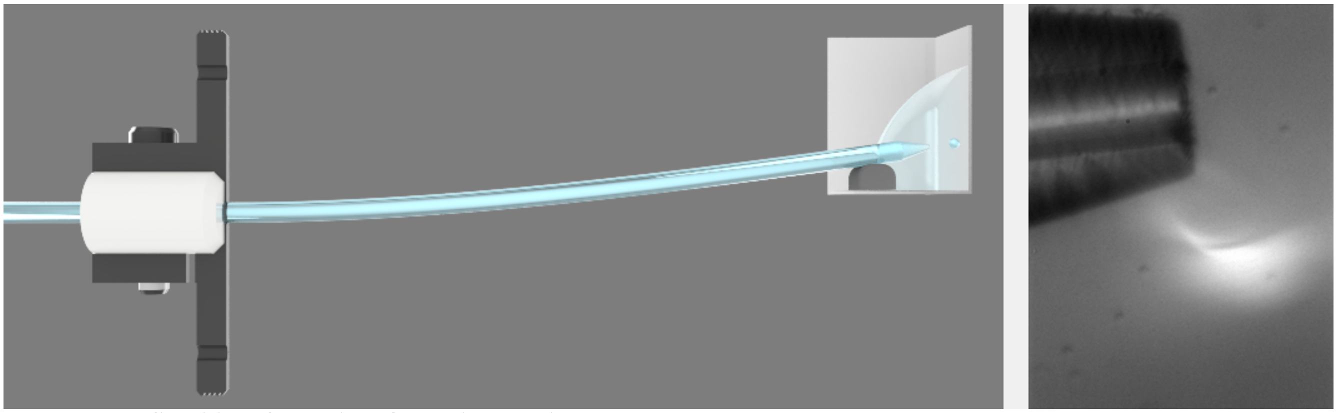

Figure SM5 | **Stability of a static HOT while bending the MMF.** A silica microsphere (1.5 µm diameter in a water suspension) remains confined in the trap site while the MMF is bent upwards. The unheld fibre portion is ≈15 mm long and the fibre endface is translated by ≈2 mm. During the recording, the imaging lens is repositioned in order to keep the fibre in the field of view.

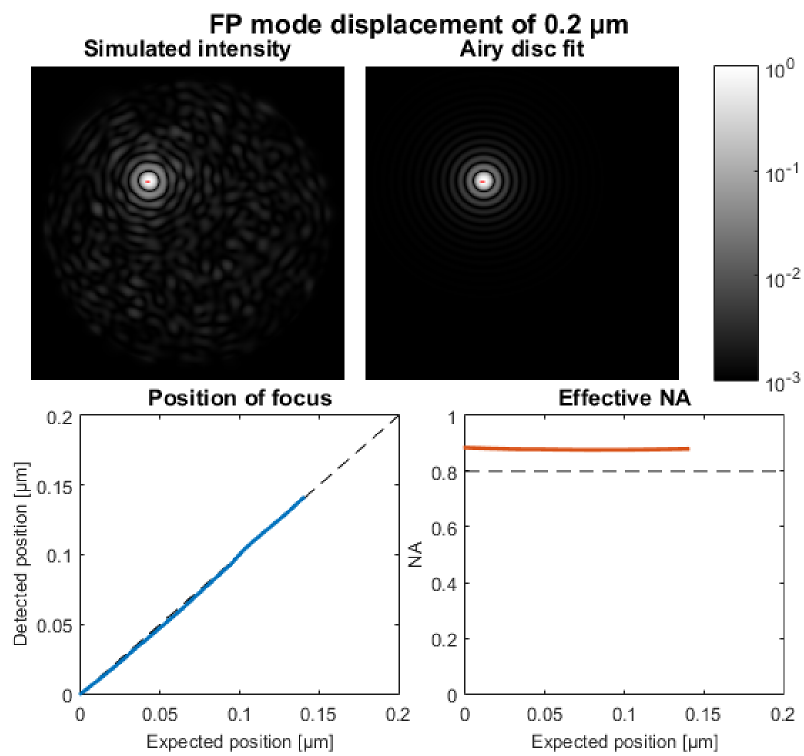

Figure SM6 | **Simulation of focus fine positioning.** Two neighbouring, diffraction-limited FP output modes separated by distances ranging from 0.1 µm to 0.8 µm are simultaneously generated. Their interference results in focus (top-left) whose central position can be finely tuned by linearly changing the relative amplitudes of two FP modes generated. By fitting a Airy disc distribution to the resulting intensity profile (top-right) we retrieve the position (bottom-left) and effective NA (bottom-right) of the focus generated. The horizontal dashed line indicates the NA value of 0.8 necessary for stable optical confinement, whereas the red line highlights the trajectory of central position of the focus.